buildings

MDPI

Article

Elastic–Plastic Fracture Analysis on Defective Q345 Steel in the Process of Small-Scale Creep Crack Propagation

Huajing Guo [1], Wenjie Tang [1], Xiaolong Tong [1,*] and Bin Sun [2,*]

[1] College of Civil Engineering and Architecture, Hunan Institute of Science and Technology, Yueyang 414006, China; 12020006@hnist.edu.cn (H.G.); twj810229604@163.com (W.T.)
[2] Department of Engineering Mechanics, Jiangsu Key Laboratory of Engineering Mechanics, Southeast University, Nanjing 210096, China
* Correspondence: 12009016@hnist.edu.cn (X.T.); sunb@seu.edu.cn (B.S.)

Abstract: Q345 steel is usually used on structures working under high temperature where creep deformation could endanger their structural integrity. In order to support the application of steel structures made of Q345 under high temperature, a fracture analysis on defective Q345 steel in the process of small-scale creep crack propagation has been performed. Three-dimensional finite element models with a semi-elliptical surface crack have been established, and the crack propagation process of Q345 steel has been simulated at 400 °C. The constraint effect near the crack tip in the process of creep crack propagation has been analyzed using the J-A_2 two-parameter method in which the influence of the crack aspect ratio, loading level, and biaxial loading ratio was studied. The previously developed constraint-based R6 procedure was adopted to assess the structural integrity of the cracked structure under small-scale creep conditions. The results showed that small-scale creep crack propagation behavior exhibits great influence on both crack tip fields and a constraint effect near the crack tip. The increase in the biaxial loading ratio, loading level, and aspect ratio of the crack could lead to an increase in the J integral, an enhancement of the constraint effect, and a decrease in the safe area in the failure assessment diagram for the cracked structure in the process of small-scale creep crack propagation.

Keywords: small-scale creep; crack propagation; defective Q345 steel; constraint effect; structural integrity

check for updates

Academic Editors: Mizan Ahmed, Chaopeng Xie, Mehran Khan, Tonghao Zhang and Abasal Hussain

Received: 21 April 2025
Revised: 9 May 2025
Accepted: 13 May 2025
Published: 15 May 2025

Citation: Guo, H.; Tang, W.; Tong, X.; Sun, B. Elastic–Plastic Fracture Analysis on Defective Q345 Steel in the Process of Small-Scale Creep Crack Propagation. *Buildings* **2025**, *15*, 1662. https://doi.org/10.3390/buildings15101662

Copyright: © 2025 by the authors. Licensee MDPI, Basel, Switzerland. This article is an open access article distributed under the terms and conditions of the Creative Commons Attribution (CC BY) license (https://creativecommons.org/licenses/by/4.0/).

1. Introduction

Q345 steel has been widely applied in steel structures working under high temperatures that could reach the critical creep temperature of the metal. In practice, it is common to detect a crack in in-service steel structures. In addition, creep deformation generally exhibits significant influence on crack tip fields and crack propagation behavior, which may lead to the fracture failure of cracked steel structures. Therefore, analysis on the creep crack propagation behavior of defective Q345 steel is urgently needed to guarantee the structural integrity of steel structures with defects under high temperatures.

Up to now, much attention has been paid to the mechanical performance of Q345 steel. Dong et al. [1] proposed a fatigue crack growth model for Q345 steel based on fracture mechanics and carried out low-cycle fatigue crack propagation experiments for a CT specimen made of Q345 steel. Dicecco et al. [2] performed high-cycle fatigue tests for Q345 steel subjected to immersion corrosion to study the influence of material degradation on the fatigue life of mining wheels. Al-azzani et al. [3] put forward a consistent creep model for Q345 steel and studied the critical temperature of restrained steel beams in fire

conditions based on finite element numerical results. Zhang et al. [4] conducted fatigue tests for Q345 steel after natural cooling from the elevated temperatures and analyzed the influence of elevated temperatures on the fatigue performance of Q345 steel using an improved single-point group testing method. Guo et al. [5] carried out a series of fatigue tests for Q345 steel after fire and studied the typical fracture failure mechanism of the specimens by scanning electron microscope and metallurgical microscopy. Zhao et al. [6] conducted axial tensile experiments for corroded Q345 steel specimens and analyzed the residual mechanical behavior of Q345 structural steel after corrosion. Chen et al. [7] carried out a series of axial compression tests to investigate the buckling behavior of Q345 LAS columns and established an accurate finite element model of the Q345 LAS column. Gao et al. [8] studied the fracture morphology of the Q345/316 L dissimilar steel welded joints and analyzed the mechanism of improving the impact toughness based on Charpy impact tests and scanning electron microscopy. Weng et al. [9] analyzed the failure competition mechanism and fatigue life assessment of Q345 steel filet welded joints under the cyclic force-controlled mode based on fatigue tests. However, the majority of current studies on Q345 steel tend to analyze the fatigue mechanism, fatigue performance, and creep behavior of Q345 steel without defects. There are few studies concentrated on the fracture behavior of defective Q345 steel in the process of creep crack propagation.

In general, the safe running of steel structures with defects is ensured using structural integrity assessment results based on fracture mechanics. The R6 procedure is a common fitness-for-service methodology to assess structural integrity using a failure assessment diagram (FAD), for which three options are provided. Li et al. [10] developed structural integrity assessment limit load solutions for plates containing embedded cracks, given in the current R6 procedure, based on finite element fracture analyses. Guo et al. [11] proposed a novel procedure to evaluate the performance of failure assessment models by investigating the integrity assessment of pipes containing axial-oriented part-through cracks on the outer surface. Lei et al. [12] investigated the effect of global and local limit load solutions for defective elbows on the reference stress and the J integral based on the R6 procedure. Fasun et al. [13] analyzed the structural integrity of a howitzer cannon barrel using the R6 procedure and determined the critical pressures concerning varying crack shapes and depths. In fact, the constraint effect near the crack tip is used to describe the independence of fracture toughness on the loading factors and crack configurations. Studies [14,15] demonstrated that the structural integrity of cracked structures can be greatly affected by the constraint effect. Guo et al. [16] modified the R6 criterion with consideration of the constraint effect and assessed the structural integrity of existing crane runway girders with defects under different working conditions. Huang [17] proposed a correction model of the FAD in a small-scale yielding condition using crack tip plasticity theories in which the constraint effect was considered. In the authors' previous work [18], a constraint-based R6 criterion was developed to assess the structures in process crack propagation, and the integrity assessment of a plate with a growing crack was performed at room temperature. However, the majority of papers are concentrated on the assessment of cracked structures with a static crack at room temperature, and there is a lack of studies assessing the structural integrity of cracked structures made of Q345 steel at high temperatures.

In practice, the finite element method has been regarded as an effective and economical analytical method, which has been widely applied to analyze the performance of materials and structures. Qian et al. [19] investigated the structural integrity of a reactor pressure vessel subjected to pressurized thermal shocks by considering the constraint effect using the finite element method. Li et al. [20] proposed design rules for high-pressure cavity assembly in which the temperature field of each assembly was visualized via the finite element method. Guo et al. [21] conducted fatigue prognosis analysis on the cracked

steel crane runway girders under high temperature using the finite element method. Liu et al. [22] performed a modal analysis of a high-temperature superconducting motor by simplifying the whole machine finite element model. Sun et al. [23] proposed a model-driven and data-driven fusion prediction framework for the fire damage evaluation of concrete structures using the finite element method.

Therefore, although many efforts have been made on the mechanical behavior of Q345 steel, the fracture problem of defective Q345 steel in the process of small-scale creep crack propagation has not been resolved yet. In this paper, it is assumed that the J integral can describe crack tip fields in small-scale creep conditions. The creep crack propagation process of defective Q345 steel has been simulated using the finite element method. The constraint effect near the crack tip in the process of creep crack propagation has been analyzed using the J-A_2 two-parameter method, in which the influence of the crack aspect ratio, loading level, and biaxial loading ratio was studied. The previously developed constraint-based R6 procedure was adopted to assess the structural integrity of the cracked structure made of Q345 steel under small-scale creep conditions.

2. The Fracture Mechanics Theories

According to fracture mechanics [24], stress intensity factor K is used to express the elastic crack tip fields, and the mode I of K for the three-dimensional semi-elliptical surface crack can be expressed as

$$K = M_f \frac{p\sqrt{\pi a}}{E(k)} \left(\sin^2\theta + \frac{a^2}{c^2}\cos^2\theta\right)^{1/4} \tag{1}$$

where $E(k)$ is the elliptic integral of the second kind, p is the applied load, M_f is the shape factor, and θ is the crack angle.

The J integral is a path-independent fracture parameter that was developed by Rice [25] to describe the elastic–plastic crack tip fields, and it can be expressed as follows:

$$J = \int_{\Gamma} \left(Wdy - T_i \frac{\partial u_i}{\partial x} ds\right) \tag{2}$$

where W is strain energy density, Γ is a path through the crack, Ti is the tension vector, u_i is the displacement vector, and ds is a microarc on the integral path.

Yang et al. [26] and Chao et al. [27] put forward J-A_2 three-term solutions to express the crack tip fields in which the constraint effect level was described by parameter A_2.

$$\frac{u_i}{\alpha\varepsilon_s L} = A_1^n \left[\left(\frac{r}{L}\right)^{ns_1+1} \widetilde{u}_i^{(1)}(\theta, n) + A_2\left(\frac{r}{L}\right)^{(n-1)s_1+s_2+1} \widetilde{u}_i^{(2)}(\theta, n) + A_2^2\left(\frac{r}{L}\right)^{(n-1)s_1+s_3+1} \widetilde{u}_i^{(3)}(\theta, n)\right] \tag{3a}$$

$$\frac{\varepsilon_{ij}}{\alpha\varepsilon_s} = A_1^n \left[\left(\frac{r}{L}\right)^{ns_1+1} \widetilde{\varepsilon}_{ij}^{(1)}(\theta, n) + A_2\left(\frac{r}{L}\right)^{(n-1)s_1+s_2+1} \widetilde{\varepsilon}_{ij}^{(2)}(\theta, n) + A_2^2\left(\frac{r}{L}\right)^{(n-1)s_1+s_3+1} \widetilde{\varepsilon}_{ij}^{(3)}(\theta, n)\right] \tag{3b}$$

$$\frac{\sigma_{ij}}{\sigma_s} = A_1 \left[\left(\frac{r}{L}\right)^{s_1} \widetilde{\sigma}_{ij}^{(1)}(\theta, n) + A_2\left(\frac{r}{L}\right)^{s_2} \widetilde{\sigma}_{ij}^{(2)}(\theta, n) + A_2^2\left(\frac{r}{L}\right)^{s_3} \widetilde{\sigma}_{ij}^{(3)}(\theta, n)\right] \tag{3c}$$

where $\widetilde{u}_i(\theta, n)$, $\widetilde{\varepsilon}_{ij}(\theta, n)$, and $\widetilde{\sigma}_{ij}(\theta, n)$ are angular displacement, angular strain, and angular stress distribution function, respectively, and r is the distance from the crack tip, σ_{ij} is the stress tensor, n is the material exponent, L is the characteristic length, and s_i is the exponent of stress function.

In the authors' previous work [18], a constraint-based J_{m} integral was put forward:

$$J_{\mathrm{m}} = \frac{J}{\beta}\left(\frac{\widetilde{\sigma}_{ij}^{(1)}(\theta) + A_2 r^{s_2-s_1}\widetilde{\sigma}_{ij}^{(2)}(\theta) + (A_2)^2 r^{s_3-s_1}\widetilde{\sigma}_{ij}^{(3)}(\theta)}{\widetilde{\sigma}_{ij}^{(1)}(\theta)}\right)^{n+1} \tag{4}$$

where β is the normalized constraint factor.

The R6 two-criterion procedure is a fitness-for-service method which is widely used to assess the structural integrity of flawed structures using the FAD. There are three failure regions in which FADs are dominated by brittle fracture, elastic–plastic deformation, and plastic collapse, respectively, as shown in Figure 1. In the FAD, the safe area illustrates that all the points (K_{r}, L_{r}) are in the inner failure curves, which implies that the flawed structure is in good working condition.

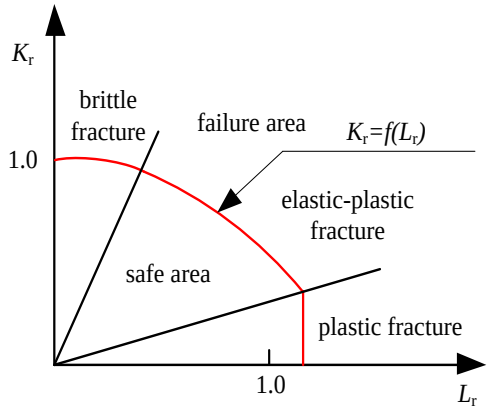


Figure 1. Schematic diagram of the FAD.

Three options are provided in the R6 procedure, and the curve of option 3 in the FAD is characterized by the horizontal axis *L*r and vertical axis *K*r [28]:

$$L_{\mathrm{r}} = \frac{p}{p_{\max}} \tag{5}$$

$$K_{\mathrm{r}} = f_3(L_{\mathrm{r}}) = \sqrt{\frac{J_{\mathrm{e}}}{J}} \tag{6}$$

where $p_{\max}$ is the limited load and J_{e} is the elastic J integral.

In the authors' previous work [18], the equivalence principle of the stress intensity factor was developed to assess the cracked structures in the process of crack propagation. The horizontal axis *L*r of option 3 in the FAD was modified as follows:

$$L_{\mathrm{r}} = \frac{p}{p_{\max}} = \frac{p_1 Y_1 / Y_i\sqrt{a_1/a_i}}{p_1 Y_1 / Y_{\max}\sqrt{a_1/a_{\max}}} = \frac{Y_{\max}}{Y_i}\sqrt{a_i/a_{\max}}\ (i = 1,\ 2,\ 3,\ \ldots, nn) \tag{7}$$

The vertical axis *K*r of option 3 in the FAD was modified to consider the constraint effect near the crack tip, and it was expressed as follows:

$$K_{\mathrm{r}} = f_3(L_{\mathrm{r}}) = \sqrt{\frac{J_{\mathrm{e}}(a,p)}{J_{\mathrm{K}}}} \tag{8}$$

3. The Finite Element Models

In this paper, three-dimensional finite element models with a semi-elliptical surface crack were established, and the crack propagation process of Q345 steel under small-scale

creep conditions has been simulated using code ABAQUS 6.14. The creep strain of metallic materials can be generated once the environmental temperature reaches about 30% of their melting point. In practice, Q345 steel could serve in extreme working conditions where the temperature reaches 400 °C [21,29]. The studied temperature was chosen as 400 °C to satisfy the small-scale creep condition. The models were subjected to biaxial tensile loading, and the geometric configurations of the plate are shown in Figure 2, where the width $2W_0$ = 100 mm, the thickness H_0 = 50 mm, and the length $2L_0$ = 100 mm.

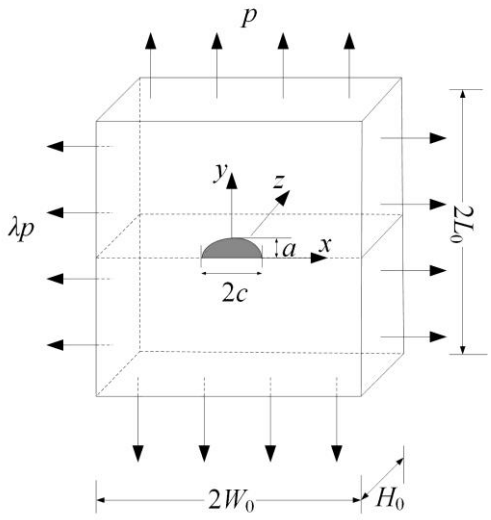


Figure 2. The geometric configurations of the three-dimensional plate.

It was assumed that the J integral can describe crack tip fields in small-scale creep conditions and the mechanical behavior of Q345 steel at high temperatures can be expressed by the Ramberg–Osgood power law:

$$\frac{\varepsilon}{\varepsilon_s} = \frac{\sigma}{\sigma_s} + \alpha\left(\frac{\sigma}{\sigma_s}\right)^n \tag{9}$$

where σ_s is the yield stress, ε_s is the yield strain, E is the Young's modulus, α is the material constant, and n is the strain-hardening exponent.

On the basis of the test data of Q345 steel at 400 °C in the reference [30], the material parameters of Q345 steel in the simulation can be obtained by the fitting method, namely, α = 1.0 and n = 7.2. According to the test data [30], the elastic modulus E = 174 GPa and the yield stress σ_s = 283 MPa at 400 °C. Note that fracture mechanics theories were used in this paper, in which the microstructure factors were not considered.

Based on the geometric symmetry of the structure, only one quarter of the plate was modeled. In the finite element simulation, symmetric conditions were applied to the sides of the model. Note that the 20-node hexahedron element (C3D20) was selected for the analysis to simulate the stress singularity. It was assumed that the initial crack length $2c_0$ = 2 mm and the aspect ratio a/c of the crack remains constant in the process of crack propagation. To be concise, only the finite element model with an initial crack is displayed in Figure 3. In the finite element model with an initial crack, the number of elements was 35,404, and the number of nodes was 147,751. The information of mesh size can be directly extracted from the finite element models using code ABAQUS. The q vectors of code ABAQUS were used to define the crack propagation direction. In addition, 6 contours around the crack tip were used in the simulation, and the average value of the J integral and K was calculated by using the results extracted from the outer 5 contours.

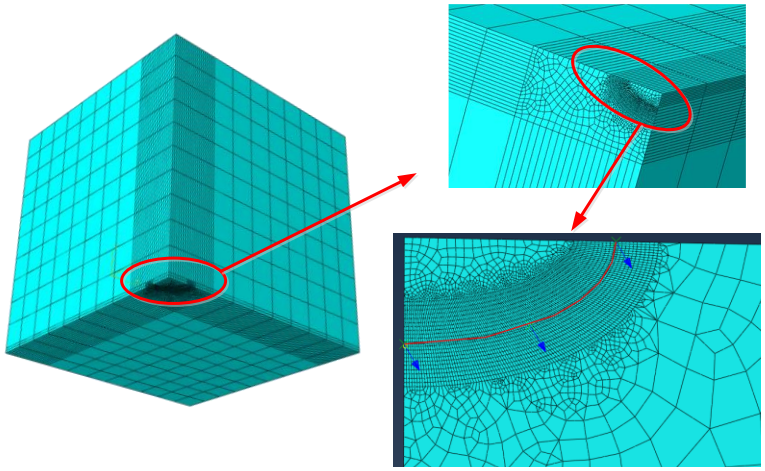


Figure 3. The finite element model with an initial crack.

The finite element software ABAQUS enables the direct extraction of the stress intensity factor solutions from the simulation results, namely finite element solutions. The stress intensity factor solutions can be calculated using Equation (1), namely theoretical solutions. In fact, Equation (1) for stress intensity factor K has been widely used in both engineering problems and theoretical research, and reliability can be guaranteed. In this study, the validity of the finite element models was verified by comparing the finite element solutions and theoretical solutions for the stress intensity factor. The solutions for the stress intensity factor at the deepest point ($\theta = 90°$) were listed in Table 1; the relative difference between the two kinds of solutions was acceptable, which guaranteed the reliability of the finite element models. Therefore, finite element numerical results and the conclusion based on the numerical results were reliable.

Table 1. Solutions for the stress intensity factor.

Crack Depth	Aspect Ratio	Applied Loading	Theoretical Solutions	Finite Element Solutions	Relative Difference
a = 1 mm	a/c = 1	p = 100 MPa	116.2	117.3	−0.93%
a = 3 mm	a/c = 1	p = 100 MPa	201.3	200.2	0.55%
a = 5 mm	a/c = 1	p = 100 MPa	259.9	260.8	−0.35%
a = 7 mm	a/c = 1	p = 100 MPa	307.5	310.5	−0.98%
a = 10 mm	a/c = 1	p = 100 MPa	367.5	375.6	−2.20%

4. The Numerical Results and Discussion

4.1. Analysis of J Integral in Creep Crack Propagation Process

In this section, the J integral was chosen to describe the crack tip fields of defective Q345 steel in small-scale creep conditions. The shape characters of the semi-elliptical surface crack were expressed by an aspect ratio a/c. Three groups of cracks with different aspect ratios have been investigated, in which the influence of the biaxial loading ratio λ was studied. The J integral near the crack tip of defective Q345 steel was directly extracted from the finite element simulation results at 400 °C, and the results are shown as Figures 4 and 5. Furthermore, the influence of the constraint effect near the crack tip on the J integral has been investigated, as shown in Figure 6. The conclusions can be obtained from Figures 4–6:

(1) The influence of the biaxial loading ratio on the J integral was slight for relatively low stress levels, and it gradually became prominent with the improvement in the stress level.

(2) The value of the J integral increased with the increase in the crack length growth and the aspect ratio of the semi-elliptical surface crack, in which the relative increase could reach 52.2%.

(3) The constraint effect near the crack tip exhibited significant influence on the *J* integral, and the maximal relative increase was 67.9% in this study, which implies that the constraint effect should be considered in the structural assessment using the J-based procedure.

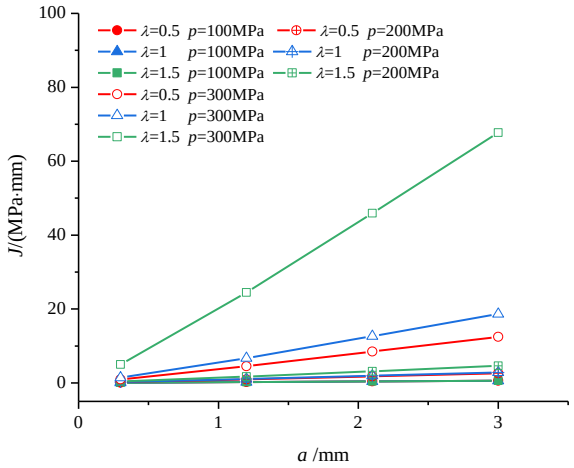


Figure 4. The influence of the biaxial loading ratio on the *J* integral.

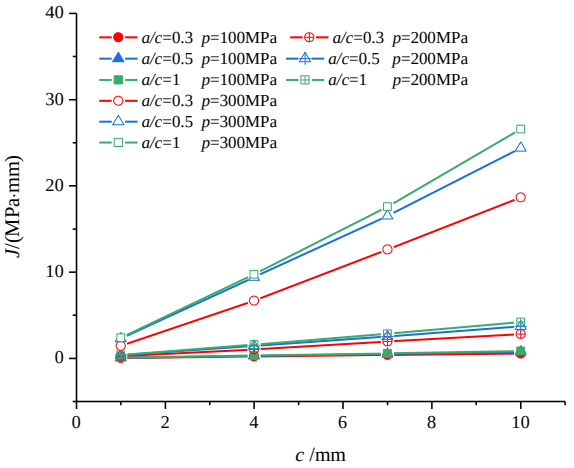


Figure 5. The influence of the aspect ratio on the *J* integral.

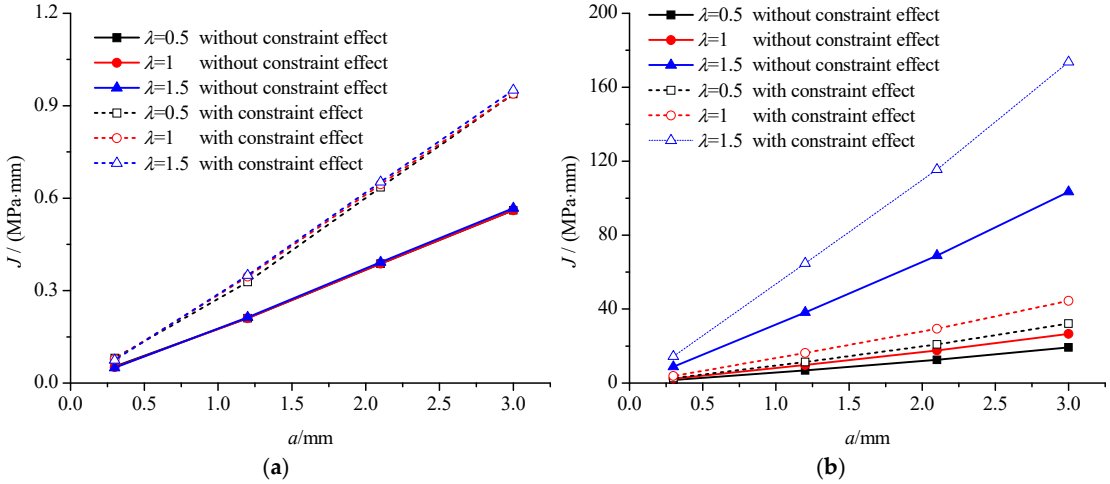


Figure 6. The influence of the constraint effect on the *J* integral: (**a**) p = 100 MPa and a/c = 0.3; (**b**) p = 300 MPa and a/c = 1.

4.2. Analysis of Constraint Effect on Creep Crack Propagation Process

On the basis of the finite element simulation results and J-A_2 three-term solutions, an analysis on the constraint effect near the crack tip in the process of creep crack propagation has been performed using the J-A_2 two-parameter method, in which the influence of the crack aspect ratio, loading level, and biaxial loading ratio was studied. The A_2 was used to describe the constraint effect level near the crack tip, and the solution was taken at a normalized distance $r/(J/\sigma_s) = 2$ from the crack tip. The numerical results are shown as Figures 7–9.

The conclusions can be obtained based on Figures 7–9:

(1) A high constraint effect level occurred near the crack tip of Q345 steel in small-scale creep conditions, and the influence of the constraint effect on crack tip fields could be enhanced due to crack growth.

(2) The influence of the biaxial loading ratio on the constraint effect level was slight for relatively low stress, levels and it gradually became prominent with the increase in the stress level in small-scale creep conditions.

(3) The constraint effect level could be improved with the increase in the aspect ratio of the semi-elliptical surface crack and applied loading level.

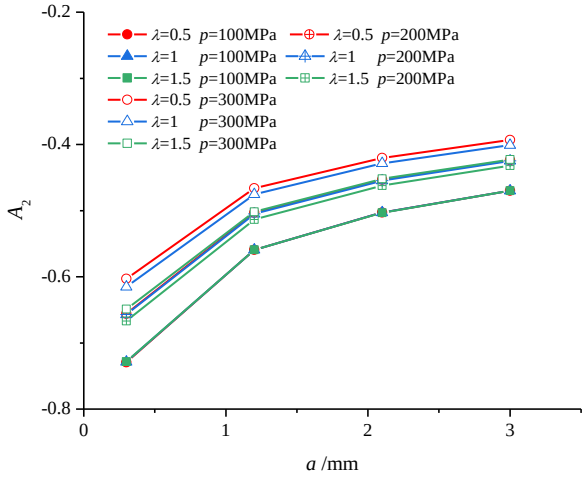


Figure 7. The influence of the biaxial loading ratio on the A_2.

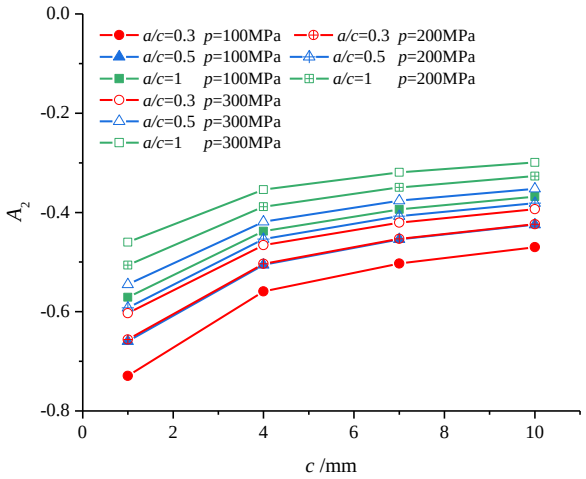


Figure 8. The influence of the aspect ratio on the A_2.

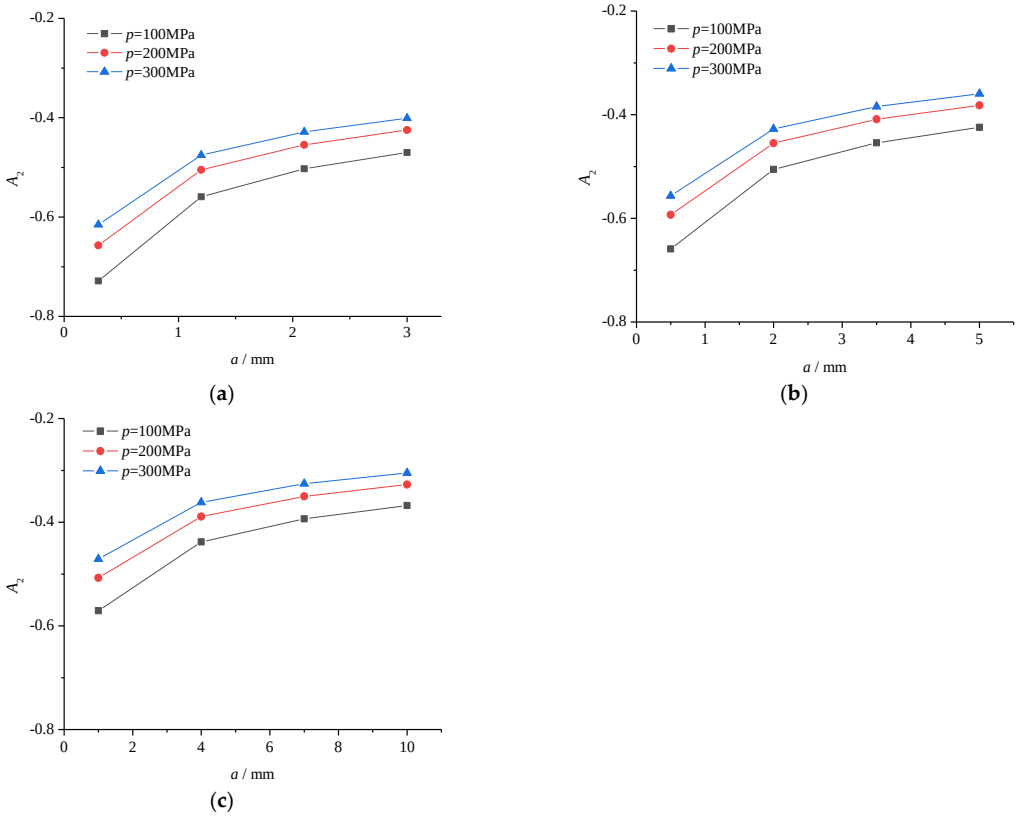


Figure 9. The influence of the loading level on the A_2: (**a**) a/c = 0.3 and λ = 0.5; (**b**) a/c = 0.5 and λ = 0.5; (**c**) a/c = 1 and λ = 0.5.

4.3. Structural Integrity Assessments for the Flawed Structure

In the previous paper [18], a modified option 3 of R6 was developed in which the influence of the constraint effect and crack growth was considered, and the horizontal axis Lr and vertical axis Kr of option 3 in the FAD were expressed by Equation (7) and Equation (8), respectively. In this section, the modified option 3 of R6 was chosen to assess the structural integrity of the flawed structure made of Q345 steel in small-scale creep conditions. On the basis of the numerical results, the structural integrity assessments for the three-dimensional plates with a semi-elliptical surface crack were performed in which the influence of the biaxial loading ratio, the aspect ratio of the crack, and the loading level was studied, and the assessment results are shown as Figures 10–12, respectively.

The conclusions can be obtained based on Figures 10–12:

(1) The safe area in the FAD decreased with the increased biaxial loading ratio, and the influence could be more prominent with the increase in the stress level.

(2) The decrease in the safe area in the FAD could occur due to an increase in the aspect ratio of the crack in the process of creep crack propagation, which could endanger the structural integrity of the structure.

(3) The increase in the loading level could lead to a decrease in the safe area in the FAD, in which the influence may be sharply enhanced due to high stress levels, and the maximal relative increase was 58.1% in this study.

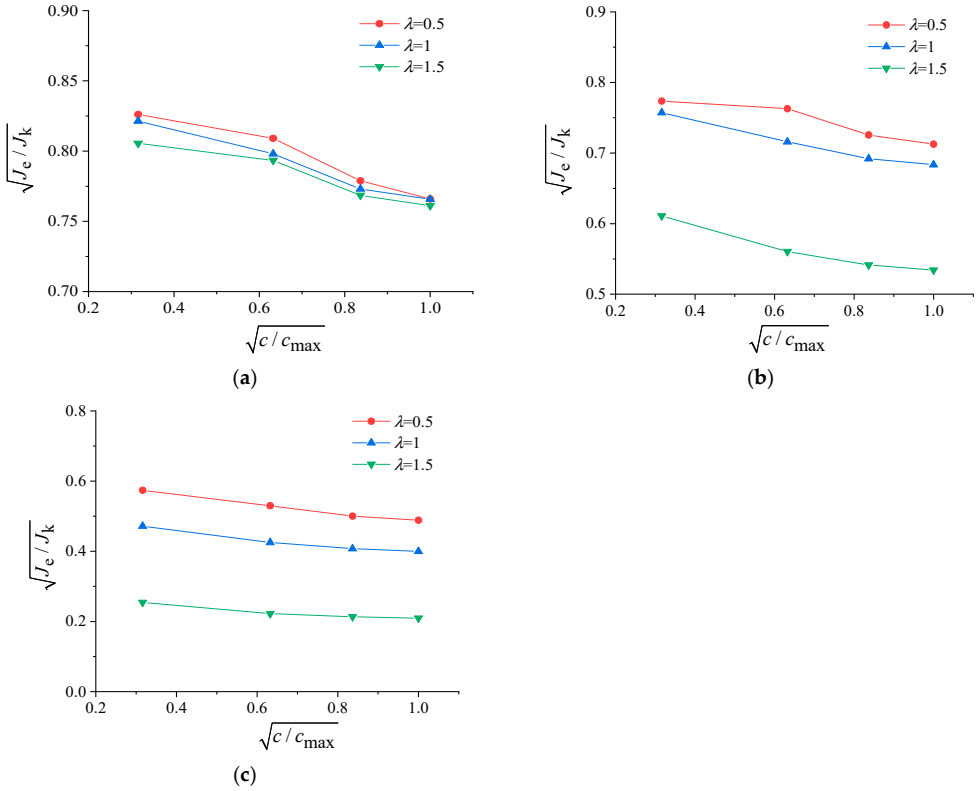


Figure 10. The structural integrity assessment curves for the structure with different biaxial loading ratios: (**a**) p = 100 MPa and a/c = 0.3; (**b**) p = 200 MPa and a/c = 0.5; (**c**) p = 300 MPa and a/c = 1.

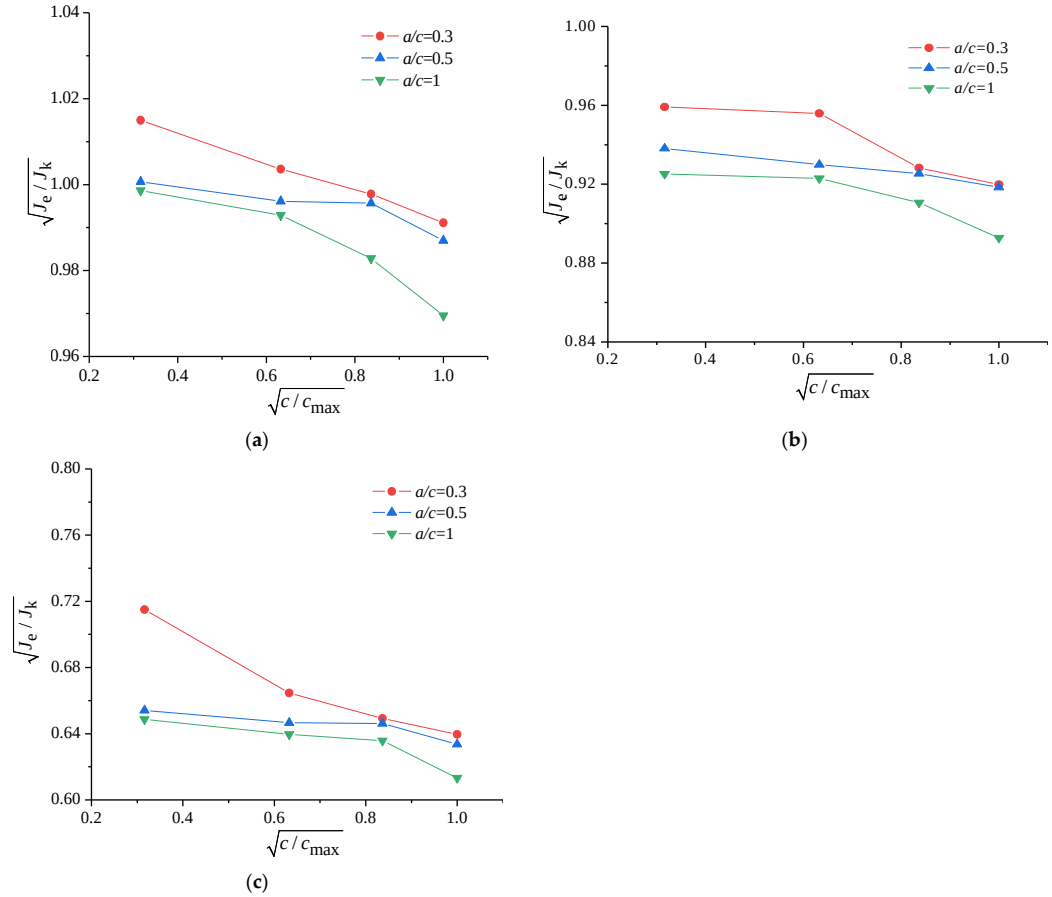


Figure 11. The structural integrity assessment curves for the structure with different crack aspect ratios: (**a**) p = 100 MPa and λ = 0.5; (**b**) p = 200 MPa and λ = 0.5; (**c**) p = 300 MPa and λ = 0.5.

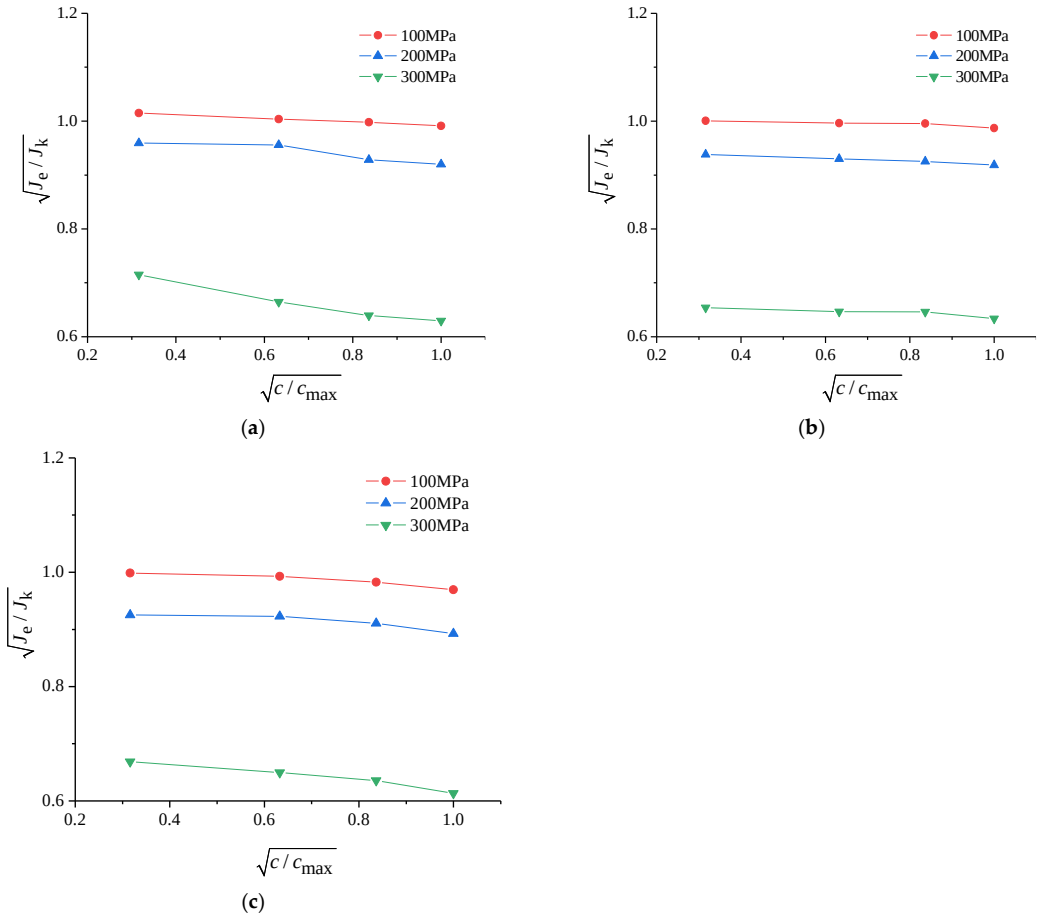


Figure 12. The structural integrity assessment curves for the structure under different working loading: (**a**) a/c = 0.3 and λ = 0.5; (**b**) a/c = 0.5 and λ= 0.5; (**c**) a/c = 1 and λ = 0.5.

5. Conclusions

This paper aimed to resolve the fracture problem of defective Q345 steel in small-scale creep conditions, and the creep crack propagation process was simulated at 400 °C. It is assumed that the J integral can describe crack tip fields in small-scale creep conditions. The constraint effect near the crack tip in the process of creep crack propagation was analyzed using the J-A_2 two-parameter method, and the structural integrity of the cracked structure subjected to biaxial loading was assessed. The main works and conclusions were summarized as follows:

(1) The increase in the aspect ratio of the semi-elliptical crack and biaxial loading ratio could lead to an increase in the J integral in small-scale creep conditions, in which the relative increase could reach 52.2% in this study.

(2) A high constraint effect level could occur near the crack tip of defective Q345 steel and the constraint effect could be enhanced due to crack growth, leading to a significant increase in the J integral, and the maximal relative increase was 67.9% in this study, which demonstrates that the constraint effect should be considered in the structural integrity assessment for the structures made of Q345 steel.

(3) The constraint effect level near the crack tip could be distinctly affected by the aspect ratio of the semi-elliptical crack, applied loading level, and biaxial loading ratio. The influence of the biaxial loading ratio on the constraint effect level was slight for relatively low stress levels, and it gradually became prominent with the increase in the stress level.

(4) The structural integrity assessment curves were provided for the three-dimensional cracked structures made of Q345 steel in the process of creep crack propagation using the

previously modified R6 procedure. The safe area in the FAD decreased with the increase in the biaxial loading ratio, loading level, and aspect ratio of the crack, and the maximal relative increase was 58.1% in this study.

Author Contributions: H.G.: Investigation, Methodology, Writing, Revision; W.T.: Investigation, Writing, Revision; X.T.: Investigation, Methodology, Writing, Revision; B.S.: Investigation, Methodology, Writing, Revision. All authors have read and agreed to the published version of the manuscript.

Funding: This work was supported by the National Natural Science Foundation of China (52478312), the Natural Science Foundation of Hunan Province (2025JJ70290) and Education Department of Hunan Province (24B0616).

Institutional Review Board Statement: Not applicable.

Informed Consent Statement: Not applicable.

Data Availability Statement: The original contributions presented in this study are included in the article. Further inquiries can be directed to the corresponding authors.

Conflicts of Interest: The authors declare no conflicts of interest.

References

1. Dong, Q.; Yang, P.; Xu, G.; Deng, J. Mechanisms and modeling of low cycle fatigue crack propagation in a pressure vessel steel Q345. *Int. J. Fatigue* **2016**, *89*, 2–10. [CrossRef]
2. Dicecco, S.; Altenhof, W.; Hu, H.; Banting, R. High-cycle fatigue of high-strength low alloy steel Q345 subjected to immersion corrosion for mining wheel applications. *J. Mater. Eng. Perform.* **2017**, *26*, 1758–1768. [CrossRef]
3. Al-azzani, H.; Wang, W.; Li, X. A consistent creep model for high strength steels and numerical investigation of creep on restrained steel beams. *J. Constr. Steel Res.* **2021**, *187*, 106937. [CrossRef]
4. Zhang, C.; Liu, Y.; Huang, C. Fatigue performance of *Q*345 structural steel after natural cooling from elevated temperatures. *J. Constr. Steel Res.* **2021**, *184*, 106811. [CrossRef]
5. Guo, Y.; Fang, C.; Zheng, Y. Post-fire hysteretic and low-cycle fatigue behaviors of Q345 carbon steel. *J. Constr. Steel Res.* **2021**, *187*, 106991. [CrossRef]
6. Zhao, N.; Zhang, C.T. Experimental investigation of the mechanical behavior of corroded Q345 and Q420 Structural Steels. *Buildings* **2023**, *13*, 475. [CrossRef]
7. Chen, H.Y.; Chen, H.; Cao, K.; Guo, Y. Study on axial compression stability of Q345 large-section angle steel columns. *Buildings* **2023**, *13*, 1030. [CrossRef]
8. Gao, L.Q.; Yang, Y.C.; Gu, B.P.; Li, S.Z. Experimental and simulation analysis on the effect of vibratory stress relief on impact toughness of Q345/316L dissimilar steel welded joints. *Mater. Today Commun.* **2024**, *38*, 108084. [CrossRef]
9. Weng, S.; Meng, C.; Deng, J.H.; Zhao, L.H.; Pei, X.J.; Zhu, M.L. Fatigue life assessment of Q345 steel fillet welded joints with competitive failure modes. *Eng. Fract. Mech.* **2024**, *298*, 109913. [CrossRef]
10. Li, Y.B.; Lei, Y.B.; Gao, Z.L.; Jin, W.Y. Structural integrity assessment of plates containing embedded cracks-Part II: Developing guidance on using the limit load solutions. *Int. J. Press. Vessel. Pip.* **2021**, *194*, 104487. [CrossRef]
11. Guo, L.Y.; Markus, N.; Jing, Z. A novel procedure to evaluate the performance of failure assessment models. *Reliab. Eng. Syst. Saf.* **2022**, *226*, 108667.
12. Lei, Y.B.; Budden, P. J predictions for defective pipe elbows via the reference stress method. *J. Press. Vessel Technol.* **2022**, *144*, 031303. [CrossRef]
13. Faun, G.; Predan, J.; Gubeljak, N. A fracture-mechanics-based approach to the analysis of the structural integrity of a howitzer cannon barrel. *Trans. Famena* **2024**, *48*, 37–52. [CrossRef]
14. Matvienko, Y.G. The effect of crack-tip constraint in some problems of fracture mechanics. *Eng. Fail. Anal.* **2020**, *110*, 104413. [CrossRef]
15. Shimodaira, M.; Tobita, T.; Takamizawa, H.; Katsuyama, J.; Hanawa, S. Constraint effect on fracture behavior of underclad crack in reactor pressure vessel. *J. Press. Vessel Technol. Trans. ASME* **2022**, *144*, 011304. [CrossRef]
16. Guo, H.J.; Wu, B.J.; Li, Z.X. Integrity analysis on existing crane runway girders with defects using constraint-based R6 criterion. *SDHM Struct. Durab. Health Monit.* **2020**, *14*, 37–50. [CrossRef]
17. Huang, X.L. Constraint-corrected failure assessment diagrams based on crack tip plastic zone size. *Eng. Fract. Mech.* **2024**, *309*, 110403. [CrossRef]

18. Guo, H.J.; Tang, W.J.; Tong, X.L. A structural Integrity assessment method for civil engineering structures with a growing crack considering constraint Effect. *IAENG Int. J. Appl. Math.* 2025; *accepted with major revise*.
19. Qian, G.A.; Niffenegger, M. Integrity analysis of a reactor pressure vessel subjected to pressurized thermal shocks by considering constraint effect. *Eng. Fract. Mech.* **2013**, *112*, 14–25. [CrossRef]
20. Li, R.; Zheng, G.L.; Liu, Y.; Wang, M.; Chen, P.; Chen, M.; Zhang, Q. Finite element design of a temperature field for high-pressure diamond synthesis. *Diam. Relat. Mater.* **2016**, *69*, 133–137. [CrossRef]
21. Guo, H.J.; Tong, X.L. Fatigue prognosis analysis on the cracked steel crane runway girders under high temperature. *Int. J. Steel Struct.* **2021**, *21*, 1022–1031. [CrossRef]
22. Liu, Z.; Xiang, Y.; Zhou, Y. Finite element modeling method and modal analysis of a high temperature superconducting motor. *IEEE Trans. Appl. Supercond.* **2021**, *31*, 5206304. [CrossRef]
23. Sun, B.; Du, S.L. Kernel extreme learning machine and finite element method fusion fire damage prediction of concrete structures. *Structures* **2024**, *68*, 107172. [CrossRef]
24. Irwin, G.R. *Fracture Dynamics, Fracturing of Metals*; American Society for Metals: Cleveland, OH, USA, 1948.
25. Rice, J.R. A path independent integral and the approximate analysis of strain concentration by notches and crack. *J. Appl. Mech.* **1968**, *1*, 379–386. [CrossRef]
26. Yang, S.; Chao, Y.J.; Sutton, M.A. Higher order asymptotic crack tip fields in a power-law hardening material. *Eng. Fract. Mech.* **1993**, *45*, 1–20. [CrossRef]
27. Chao, Y.J.; Yang, S.; Sutton, M.A. On the fracture of solids characterized by one or two parameters: Theory and practice. *J. Mech. Phys. Solids* **1994**, *42*, 629–647. [CrossRef]
28. Milne, I.; Ainsworth, R.A.; Dowling, A.R.; Stewart, A.T. Assessment of the integrity of structures containing defects. *Int. J. Press. Vessel. Pip.* **1988**, *32*, 3–104. [CrossRef]
29. Wang, W.Y.; Yan, S.H.; Zhang, L.B.; Wang, B. Creep test on Q345 steel at elevated temperature and fire resistance of steel columns considering creep. *J. Build. Struct.* **2016**, *37*, 47–54.
30. Yuan, G.L.; Shu, Q.J.; Huang, Z.H.; Li, Q. An experimental investigation of properties of Q345 steel pipe at elevated temperatures. *J. Constr. Steel Res.* **2016**, *118*, 41–48. [CrossRef]

Disclaimer/Publisher's Note: The statements, opinions and data contained in all publications are solely those of the individual author(s) and contributor(s) and not of MDPI and/or the editor(s). MDPI and/or the editor(s) disclaim responsibility for any injury to people or property resulting from any ideas, methods, instructions or products referred to in the content.